Dimuon production in proton-copper collisions at $\sqrt{s}$=38.8 GeV

G. Moreno,[a] C. N. Brown, W. E. Cooper, D. Finley, Y. B. Hsiung,
A. M. Jonckheere, H. Jostlein, D. M. Kaplan,[b] and L. M. Lederman[c]
Fermilab, Batavia, Illinois 60510

Y. Hemmi, K. Imai, K. Miyake, T. Nakamura,[d]
N. Sasao, N. Tamura,[e] and T. Yoshida[f]
Kyoto University, Kyoto, 606 Japan

A. Maki and Y. Sakai
KEK, Tsukuba-gun, Ibaraki-ken, 305 Japan

R. Gray,[g] K. B. Luk,[h] J. P. Rutherfoord,[i]
P. B. Straub, R. W. Williams, and K. K. Young
University of Washington, Seattle, Washington 98195

M. R. Adams,[j] H. Glass,[k] D. Jaffe,[j] and R. L. McCarthy
State University of New York, Stony Brook, New York 11794

J. A. Crittenden[l] and S. R. Smith[m]
Columbia University, Nevis Laboratories, Irvington, New York 10533
(Received 29 October 1990)

Experimental results on the production of dimuons by 800-GeV protons incident on a copper target are presented. The results include measurements of both the continuum of dimuons and the dimuon decays of the three lowest-mass Υ S states. A description of the apparatus, data acquisition, and analysis techniques is included. A comparison of the results with data taken at lower incident energies indicates a scaling behavior of the continuum dimuon yields.

I. INTRODUCTION

The study of high-mass lepton pair production in proton-nucleus collisions has proven to be a valuable tool in understanding the internal structure of matter. In particular, the experiment of Christenson *et al.*[1] led Drell and Yan[2] to propose a model in which dimuon production occurs in lowest order by the electromagnetic annihilation of nucleon constituents. After the pioneering work of Christenson *et al.*, many other groups have studied dilepton production. Among them, the experiment of Aubert *et al.*[3] observed the J/ψ resonance and hence, hidden charm, and the experiment of Herb *et al.*[4] revealed the existence of a third generation of quarks through the discovery of the Υ resonance.

This experiment was designed to allow a precision measurement of the 7–18-GeV mass spectrum of dimuons produced in 800-GeV proton-copper collisions. A detailed description of the apparatus and the data-acquisition system are given in Sec. II. The data analysis is described in Sec. III. Results on both the continuum of dimuons and the Υ S states observed via their decay into muon pairs are presented in Sec. IV.

A. The Drell-Yan process

The Drell-Yan model[2] is the simplest description of the continuum of massive lepton pairs produced in hadronic collisions:

$$h_A + h_B \longrightarrow l^+ l^- + X \ . \tag{1}$$

As depicted in Fig. 1, this process is described as an electromagnetic annihilation of a quark (antiquark) in hadron A and an antiquark (quark) in hadron B into a lepton pair. One scaling form of the cross section for producing a dilepton of mass m and fractional longitudinal momentum x_F in the hadron-hadron center-of-mass (c.m.) frame is[5]

$$m^3 \frac{d^2\sigma}{dm\,dx_F} = \left(\frac{8\pi\alpha^2}{9}\right)\left(\frac{x_1 x_2}{x_1 + x_2}\right) \times \sum_i e_i^2 [q_i^A(x_1)\bar{q}_i^B(x_2) + \bar{q}_i^A(x_1) q_i^B(x_2)] \ , \tag{2}$$

where α is the fine-structure constant, e_i is the frac-

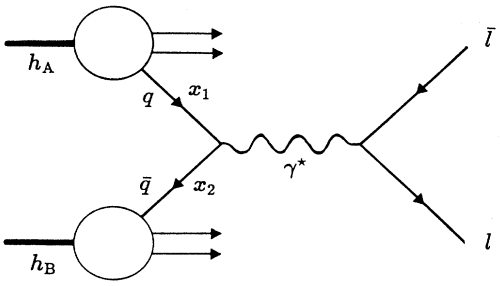

FIG. 1. The Drell-Yan process. A quark with momentum fraction x_1 in hadron A annihilates an antiquark with momentum fraction x_2 in hadron B. The virtual photon of mass $m = \sqrt{x_1 x_2 s}$ then decays into a lepton pair.

tional charge of the quark of flavor i, and $q_i^A(x_1)\,dx_1$ $[\bar{q}_i^B(x_2)\,dx_2]$ is the probability of finding quark [antiquark] i carrying a momentum fraction x_1 $[x_2]$ of the parent hadron A $[B]$. The kinematics of the process constrains the quark momentum fractions in terms of the dimensionless physical observables

$$\tau \equiv m^2/s = x_1 x_2 \ , \qquad x_F \equiv 2p_l/\sqrt{s} = x_1 - x_2 \ , \tag{3}$$

where $\sqrt{s}$ is the hadron-hadron c.m. energy and p_l is the dimuon longitudinal momentum in the c.m. frame. An alternate longitudinal variable often used instead of x_F is the rapidity

$$y = \frac{1}{2} \ln \left(\frac{E + p_l}{E - p_l} \right) \ , \tag{4}$$

where E is the dimuon energy in the c.m. system.

This Drell-Yan description further assumes that the quark distributions are the same as those measured in lepton scattering experiments and that the transverse momentum in the process is small and can be neglected by simply integrating the observed rate over the transverse momentum.

The model has received much attention because of its simplicity and striking predictions.[5] Direct comparisons of Eq. (2) with experimental data show that the measured cross section typically lies above the predicted value by a factor of about 2 (which has become known as the K factor). The angular distribution of the leptons has been measured[6] to be consistent with a $1 + \cos^2\theta$ distribution (within the uncertainties of defining the axis with respect to which θ is measured in the dilepton c.m. frame). The model cannot explain the observed large transverse momenta of dileptons, p_t, but it does assume the observed A^1 nuclear weight dependence of the cross section.[7] Also note that, for a given x_F, the right-hand side of Eq. (2) should depend on $\sqrt{\tau}$ only. This property, known as scaling, has been confirmed by experiments performed at different c.m. energies. Moreover, perturbative QCD calculations[8] have shown that order-α_s corrections to the model reproduce the K factor and explain the observed distributions at large p_t. These corrections also predict small violations of scaling since the parton distribution functions depend not only on the fractional momentum, but also on the momentum transfer in the annihilation.

B. The Υ family

The Υ family was discovered[4] in 1977 by the CFS (Columbia–Fermilab–Stony Brook) group by observing dimuons produced by 400-GeV protons. The first data gave evidence for a resonance, called the Υ, at $m \sim 9.5$ GeV. More data indicated additional resonances: the Υ' at 10.0 GeV and the Υ'' at 10.4 GeV. The Υ family is now interpreted as a bound state of the beauty quark b and its antiquark partner $\bar{b}$. The Υ states have the same quantum numbers as the photon, $J^{PC} = 1^{--}$.

Most Υ spectroscopy[9] has come from e^+e^- annihilation experiments, in which the virtual photon in the annihilation couples directly to the quarkonium system. Different production mechanisms are expected to dominate in hadronic reactions. For example, in the model of Baier and Rückl,[10] the lowest-order QCD contributions are initiated by gluons and light quarks. To order α_s^2, only the gluon-fusion process contributes and populates the low-p_t region with a mean p_t determined by the intrinsic transverse momentum of the gluons. To order α_s^3, there are many more contributions. The most important are processes in which a gluon or a quark recoils against the heavy resonance, thus leading to large transverse momenta. They also estimate that 20% of the high-p_t Υ come from radiative decays of the χ_b states.

The difference in the production mechanisms for Drell-Yan dileptons and dileptons from Υ decay should reflect itself in the measured kinematical distributions.

II. EXPERIMENTAL SETUP

A. Apparatus overview

Fermilab experiment E605 was originally designed to detect simultaneously both leptons and hadrons, which required a high incident beam flux as well as good momentum resolution and background rejection.[11] To reduce the background of charged particles coming from the interaction, a long open-aperture magnet was used to focus high-momentum particles onto the downstream detectors and to sweep away the low-momentum particles. A beam dump inside the magnet intercepted the noninteracted beam and the huge flux of low-p_t particles. A second magnet following the first detector planes aided in momentum determination and in discrimination against muons originating in the beam dump. Particle identification was done with the aid of a ring-imaging

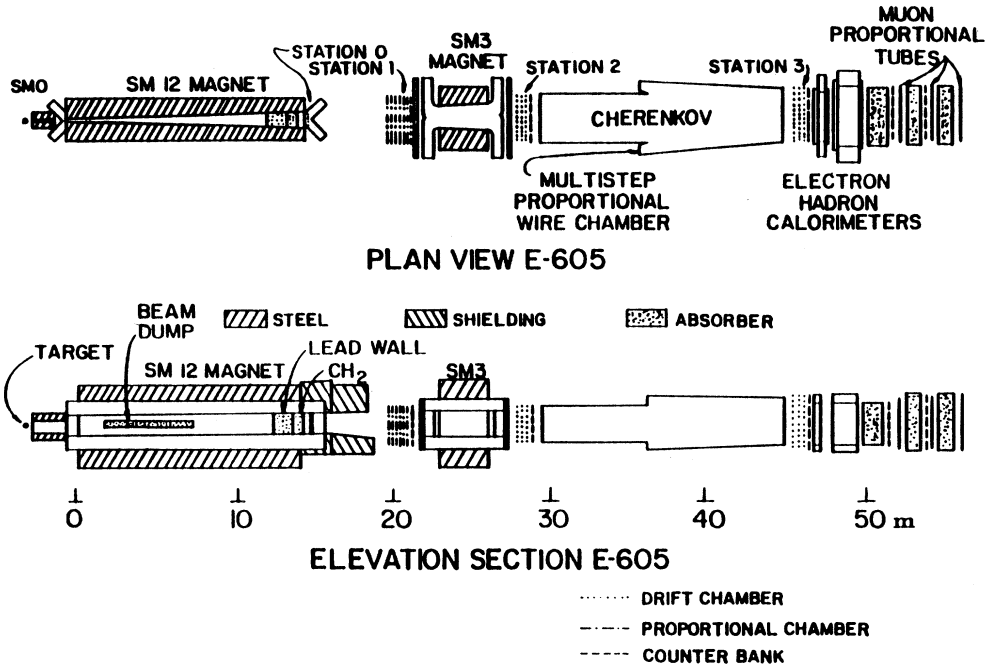

FIG. 2. The E605 spectrometer.

Cherenkov counter, hadron and electron calorimeters, and muon counters. The apparatus, shown in Fig. 2, was located in the Meson East Experimental Area of the Fermi National Accelerator Laboratory.

E605 concentrated on detecting only dimuons during the last run of the experiment. A Monte Carlo study had shown that an absorbing wall could be added, allowing higher incident intensities while maintaining excellent mass resolution. Thus, a lead wall was placed at the downstream end of the first magnet, followed by a wire chamber to allow a precise determination of the momentum using the downstream magnet only. With this modification, the apparatus was transformed into a closed-aperture focusing magnetic spectrometer for muon pairs. It covered approximately one steradian near 90° in the proton-nucleon center-of-mass system.

B. Beam and monitors

The proton beam used in this experiment was produced in bursts (rf buckets) of less than 2 ns duration separated by 19 ns during the 23-sec slow-extraction process from the accelerator. The primary proton beam was focused onto a spot 5 mm wide by 0.3 mm high full width at half maximum. The transverse position of the beam near the target was monitored by a movable segmented-wire ion chamber (SWIC). The SWIC had wires spaced 0.5 mm in the vertical direction and 2 mm in the horizontal direction.

Beam intensity per spill was measured with a secondary emission monitor (SEM) located approximately 100 m upstream of the target. The SEM was calibrated by inserting copper foils into the beam and then measuring the yield of ^{24}Na produced in the foils per SEM count. With the value of the cross section for the production of ^{24}Na in Cu by 400-GeV protons currently used at Fermilab,[12] 3.90 ± 0.11 mb, the SEM calibration constant was found to be $(0.80 \pm 0.04) \times 10^8$ protons per SEM count.

The fraction of beam protons hitting the target (targeting efficiency) was monitored with a fourfold scintillation telescope viewing the target at 90° in the lab through a small hole in the concrete shielding which enclosed the target area.

C. Targets

Table I lists some properties of the two targets used in the experiment. Both targets were thin sheets of copper with vertical thicknesses as listed in the table and hori-

TABLE I. Parameters of the targets.

	10 mil	17 mil
Thickness (mm)	0.254	0.432
Length (mm)	38.1	31.75
Width (mm)	38.0	38.0
Density (g/cm^3)	8.96	8.96
Atomic weight A	63.54	63.54
Atomic number Z	29	29

zontal widths of 3.8 cm. Since the targets were vertically slightly thinner than the beam, the vertical interaction position was very well defined. On the other hand, the horizontal size of the interaction region was determined by the width of the beam.

The targets were mounted 2.54 cm apart vertically on a movable holder in a vacuum target box. A precision motor-driven platform supported the target holder such that the vertical and horizontal position of the target could be remotely controlled.

D. Magnets

Two dipole magnets (SM12 and SM3) were used in our experiment. The SM12 and SM3 magnetic fields were oriented horizontally but in opposite directions. SM12 was used to focus high-p_t particles into the spectrometer while SM3 was used to measure their momenta.

1. SM12, beam dump, and absorbers

The upstream face of the SM12 yoke was chosen to be the z=0 plane in the E605 reference frame: we defined the z axis along the beam direction, the y axis pointing vertically upwards, and the x axis horizontal forming a right-handed system. The x and y coordinates were measured from the beam line. Thus, the nominal target position (in meters) was (0, 0, −3.3).

SM12 was 14.4 m long, 2.7 m wide, and 5.2 m high, with an aperture 0.93 m wide by 1.22 m high and was made of 1200 tons of iron blocks and four conventional water-cooled aluminum coils.[13] It was operated at two settings, imparting a transverse momentum kick of 7.5 GeV at 4000 A and 5.6 GeV at 2750 A.

Seven iron poleface modules were inserted in SM12 to increase the field intensity by tapering the magnetic volume horizontally from 15.24 cm at the entrance to 93.0 cm at the exit. Each module held lead and tungsten absorbers on its upper and lower surfaces to absorb low-energy particles. The second and third upstream modules supported the beam dump that covered the horizontal aperture from $y = -15.2$ cm to $y = +15.2$ cm. The beam dump was a 4.27-m-long copper block, slightly tapered from a vertical thickness of $y = \pm 12.7$ cm at $z = 1.73$ m to $y = \pm 15.2$ cm at $z = 2.64$ m, and then remaining at a constant thickness of $y = \pm 15.2$ cm until it ended at $z = 6.00$ m. It was followed by another 1.53 m of lead and polyethylene absorbers also covering $y = \pm 15.2$ cm.

At z=12.7 m, there was a 1.2-m-thick lead wall that fully blocked the magnet aperture, absorbing all hadrons, photons, and electrons. A 0.6-m-thick borated-polyethylene wall downstream of the lead wall absorbed neutrons generated in the lead.

2. SM3

SM3 was a conventional analyzing magnet, 3.23 m long, 5.40 m high, and 2.59 m wide, with water-cooled aluminum coils. It was located between two stations of detectors in order to measure the muon momenta. An excitation current of 4200 A gave a transverse magnetic kick of 0.91 GeV. Its magnetic volume was also tapered such that the horizontal aperture was 1.35 m at the upstream end and 1.50 m at the downstream one, while the vertical aperture was 1.68 m. A polyethylene bag containing helium was used in the aperture of the magnet to reduce multiple scattering. A 5-cm-thick iron plate (with aperture cutouts) was mounted at each end to reduce the fringe field at the nearby detectors.

3. Field measurements

The magnetic fields were determined at regularly spaced points with flip-coil measurements. Field maps were then produced by interpolating and regularizing the data. The measurements attained better than 1% accuracy on the field integral and 0.2% accuracy on the shape of the major field component, as was confirmed by the subsequent measurements of the positions and widths of the Υ resonances.

E. Tracking detectors

Several wire chambers and scintillation counters were grouped together to form a detector station. There were five detector stations providing tracking information along the spectrometer. They were numbered from 0 to 4 according to their z position. Station 0 was attached to the downstream end of the SM12 yoke. Stations 1 and 2 were just upstream and downstream of SM3. A Cherenkov counter was located between stations 2 and 3. The calorimeters were positioned behind station 3, followed by a hadron absorber wall and station 4. The three planes of proportional tubes at station 4 were interspersed with zinc and concrete absorbers.

1. Hodoscopes

Hodoscope planes were included at each station, except for station 0, and their parameters are listed in Table II. All were constructed of horizontally segmented (X planes) or vertically segmented (Y planes) NE110 plastic scintillator with signals collected and amplified by Hamamatsu R239 phototubes. The hodoscopes were primarily used in the generation of the fast triggers, but were also utilized in the track-reconstruction routines to eliminate false track candidates.

2. Wire chambers

A high-rate proportional drift tube chamber (PDT) measured the y position at station 0. It had four planes of cylindrical aluminum tubes of 1 cm diameter. It was

TABLE II. Hodoscope characteristics. The widths in parentheses correspond to the outer counters only.

Detector name	z position (m)	Aperture x (m) $\times$ y (m)	Segmentation $x \times y$	Counter width (cm)
Y1	20.47	1.22 × 1.52	2 × 12	12.7
X1	20.51	1.22 × 1.52	12 × 2	10.2
Y2	28.32	1.63 × 1.73	2 × 17	10.2
X3	46.66	2.64 × 2.34	13 × 2	22.0 (11.0)
Y3	46.92	2.64 × 2.34	2 × 13	17.8 (19.1)
Y4	51.70	2.95 × 2.54	2 × 14	17.8 (20.3)
X4	54.13	3.20 × 2.90	14 × 2	20.3 (18.1)

used to measure accurately the vertical position of the possible scattering point in the lead wall.

Track reconstruction used information from stations 1, 2, and 3. The y, u, and v coordinates of the particle trajectories were measured at each station, with u and v oriented at angles of $\pm \arctan(\frac{1}{4})$ with respect to the y axis. Station 1 consisted of six multiwire proportional chambers (MWPC's) of 2-mm wire spacing. Stations 2 and 3 each had six drift chambers (DC's)—one pair for each coordinate. Each chamber pair had one plane shifted by half a cell with respect to the other to resolve the ambiguity of the drift direction. The cell size was approximately 10 mm in station 2 and 20 mm in station 3. The dimensions and measured resolution of the chambers are presented in Table III.

Three planes of proportional tubes (PTY1, PTX, and PTY2), measuring either the x and y coordinates, were used at station 4 to identify muons. An 81-cm-thick concrete wall, a 92-cm-thick zinc wall, and a 10-cm-thick lead plate, placed just downstream of the calorimeter, shielded against hadron shower leakage. Behind it, hodoscope Y4 and PTY1 were followed by 92 cm of concrete absorber, then hodoscope X4 and PTX, another 92 cm of concrete, and finally, PTY2.

TABLE III. Parameters of the wire chambers.

Detector name	type	z position (m)	Dimensions (m) $x \times y$	Channels	Cell width (mm)	Resolution μm
Y0A	PDT	14.69	1.00 × 1.22	120	10.16	400
Y0B	PDT	14.70	1.00 × 1.22	120	10.16	300
Y0C	PDT	14.71	1.00 × 1.22	120	10.16	350
Y0D	PDT	14.72	1.00 × 1.22	120	10.16	350
U1A	MWPC	18.97	1.28 × 1.51	896	1.97	640
Y1A	MWPC	19.22	1.28 × 1.50	736	2.03	640
V1A	MWPC	19.48	1.28 × 1.51	896	1.97	640
U1B	MWPC	19.73	1.28 × 1.51	896	1.97	640
Y1B	MWPC	19.98	1.28 × 1.50	736	2.03	640
V1B	MWPC	20.24	1.28 × 1.51	896	1.97	640
U2	DC	27.52	1.68 × 1.83	208	9.86	255
U2′	DC	27.58	1.68 × 1.83	208	9.86	255
Y2	DC	27.77	1.68 × 1.79	176	10.16	255
Y2′	DC	27.82	1.68 × 1.79	176	10.16	255
V2	DC	28.02	1.68 × 1.83	208	9.86	255
V2′	DC	28.08	1.68 × 1.83	208	9.86	255
U3	DC	45.76	2.69 × 2.43	144	20.21	230
U3′	DC	45.83	2.69 × 2.43	144	20.21	230
Y3	DC	46.01	2.69 × 2.33	112	20.83	230
Y3′	DC	46.09	2.69 × 2.33	112	20.83	230
V3	DC	46.26	2.69 × 2.43	144	20.21	230
V3′	DC	46.33	2.69 × 2.43	144	20.21	230
PTY1	PT	51.86	2.97 × 3.05	120	25.40	
PTX	PT	54.25	3.43 × 3.09	135	25.40	
PTY2	PT	55.90	3.59 × 3.64	143	25.42	

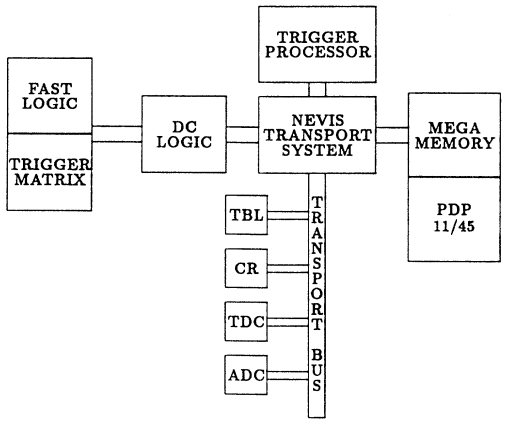

FIG. 3. Block diagram of the data-acquisition system.

F. Data acquisition

The data-acquisition system consisted of a triggering system, a readout system, a cache memory, and an on-line computer, as shown in Fig. 3. This data-acquisition system is described in detail in Ref. 14. Relevant details are presented here.

1. Triggering technique

With 2000 protons per rf bucket incident on our 0.25-interaction-length Cu target, about 500 interactions were produced every 19 ns. Three levels of triggers were employed to decide whether or not a set of tracks in the apparatus should be recorded. The first-level triggers (fast triggers) made their decision with a time resolution of less than 19 ns, rejecting pairs of tracks associated with different rf buckets. The fast triggers reduced the rate to a level where the second-level triggers (DC logic) and third-level trigger (trigger processor) could make a more detailed decision, based on tracking information, with a dead time of about 10%.

2. Fast triggers

Figure 4 is a schematic of the fast logic. Hodoscope signals were synchronized to the accelerator rf signal by the University of Washington pulse stretchers[15] and then fanned out to coincidence register (CR) cards, trigger matrix modules, multiplicity units, and hodoscope terminator modules. The terminator modules performed the logical OR of each half-bank (L=left and R=right) of counters for input to coincidence circuits set to require three of the four hodoscope planes X1, Y2, Y4, and X4. These coincidences, called $\frac{3}{4}\mu_L$ and $\frac{3}{4}\mu_R$, most often corresponded to high-momentum muons traversing the apparatus. From these, a loose dimuon trigger was formed requiring a left-right muon coincidence:[16] $\frac{3}{4}\mu_L \odot \frac{3}{4}\mu_R$. The single muon triggers (prescaled by 64 K) and the loose dimuon trigger generated a signal to start the second-level trigger cycle.

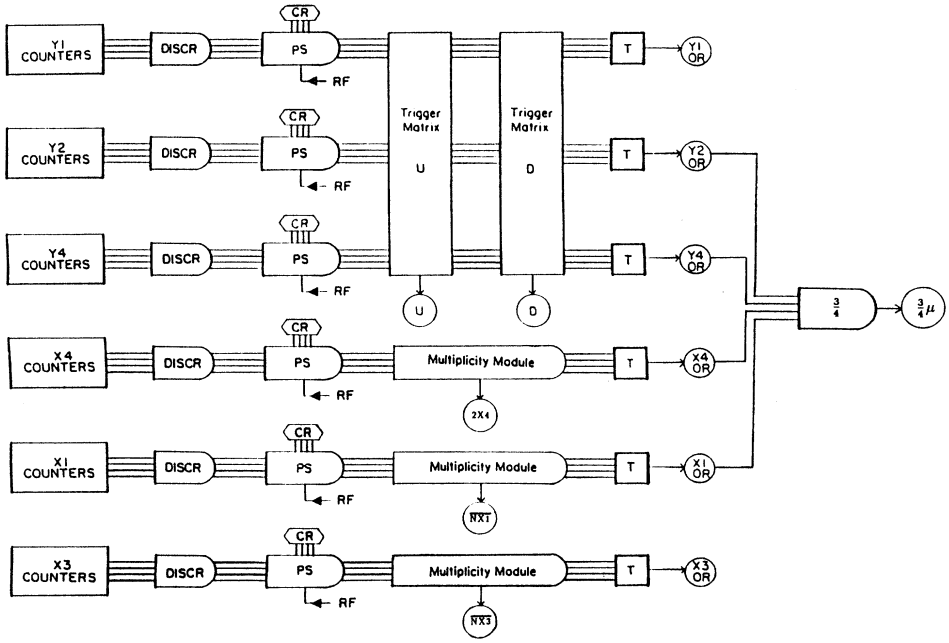

FIG. 4. Fast trigger logic. The discriminators (DISCR), pulse stretchers (PS), and terminators (T), were implemented in ECLINE circuits. The accelerator rf gate at the PS synchronized the subsequent electronics and helped achieve single rf bucket timing resolution.

3. Trigger matrix

The trigger matrix was configured to form a threefold coincidence for predetermined counter combinations in the Y1, Y2, and Y4 hodoscope planes. Four sets of hodoscope combinations (called μ matrices) crudely defined muons that went above or below the beam dump, and to the left or right side of the apparatus. μ-matrix signals were then sent to the DC logic modules for processing.

4. Multiplicity requirements

Two veto signals, called $\overline{\text{NX1}}$ and $\overline{\text{NX3}}$, were generated if more than 10 counters had fired in X1, or more than 9 in X3. Good dimuon events tended not to fire many counters. The veto efficiencies were checked by comparing multiplicity distributions for dimuon events with those of background events. The background, formed by high-multiplicity interactions of secondary and tertiary particles within the spectrometer, would otherwise overwhelm the logic.

The signal 2X4 required at least two hits in X4, with at least one being outside the two central counters (to help reject low-p_t muons from the target or beam dump). To aid in the rejection of low-p_t muons, upper and lower Y4 hodoscope counters were shortened to remove the region $\theta_x < 3$ mrad and $|y| > 62$ cm.

5. DC logic

The second-level trigger, the DC logic,[17] consisted of a flexible electronic coincidence system capable of generating up to 16 different logical trigger coincidences. The DC logic was used to implement our main data-acquisition trigger, SINK=$2\mu_{\text{matrices}} \odot 2\text{X4} \odot \overline{\text{NX1}} \odot \overline{\text{NX3}}$, and four study triggers. SINK was designed to record two opposite-sign, clean, high-p_t muons. The study triggers were prescaled until they represented less than 25% of the total number of events written to tape. The study triggers were used to check the efficiencies of the SINK components as well as the efficiencies of the trigger processor and tracking detectors.

6. Trigger processor

The trigger processor[18] was a parallel-pipeline event processor. It used hit information from eight Y chambers to find tracks in the plane of the magnetic deflection. For each track found, the y component of momentum at the target (p_y) was calculated, and a pseudomass for the event was approximated by the sum of the absolute values of the most positive and most negative values of p_y.

The final decision whether to accept or reject the event depended on trigger type. All study triggers were accepted by the processor, while for SINK triggers the pseudomass value was compared to programmable thresholds in order to accept, prescale, or reject the event.

7. Readout system

The Nevis transport system[14] formed the communications highway among the various pieces of the readout system. Transport read out all nonzero data from each element (trigger bits, hodoscope hits, chamber hits, etc.), storing the information into the temporary buffer, the megamemory. The megamemory[19] had 4 megabytes of memory and could store up to 4092 events per spill. At the end of each spill, the online computer (PDP-11/45) transferred the megamemory contents onto a 6250 BPI magnetic tape. It also performed a crude analysis of a few percent of the events in order to monitor detector efficiencies.

III. DATA ANALYSIS

A. Data reduction

Data reduction was divided into four stages, with an overall compression factor of about 600. At each stage of the analysis, all raw information on the data tape was passed forward, together with software information (positions, momenta, etc.) to an output disk file, for events which appeared to contain two good muon tracks.

The first stage was devoted to track reconstruction and muon identification. We gained a factor of about 10 in computing time by using the trigger processor information as input for the track-finding algorithm. First of all, to cleanse the data of high-multiplicity events, several multiplicity cuts were applied before the actual event selection. Hodoscope counters were used to generate trigger matrix roads of possible track candidates. Then, chamber hit windows were created at stations 1, 2, and 3, using the matrix roads. Finally, the set of y hits considered by the track-finder was restricted to those found by the on-line trigger processor inside the matrix windows. The track-finding algorithm consisted of matching upstream and downstream line segments at the SM3 bend plane and then, after a χ^2 fitting procedure, checking if the resulting trajectory was consistent with a particle originating in the target. A minimum of 11 out of 18 chamber hits at stations 1, 2, and 3 were required along each track. For each track found, at least three out of the five elements at station 4 were required for positive muon identification. Approximately 2% of all the events on a raw data tape were accepted for further analysis.

In the second stage, events clearly originating in the beam dump or scattering off the interior walls of SM12 were rejected. In the third stage, station 0 hits were added to the tracking routine to improve the knowledge both of the track momentum and the position at the lead wall.

In the last stage of the data reduction, a fine-grained SM12 field map was used to retrace muon trajectories back to the target, starting at the SM3 bend plane, and thus to obtain the production momentum vector. In addition to the target-track requirement (as explained below) and fiducial cuts, tracks were also required to have

fired the corresponding elements of the trigger matrix to ensure that the event was not triggered by accidental hodoscope hits. See the next section for the summary of cuts applied to the data.

The trace-back strategy was complicated by the presence of the absorbers blocking the downstream aperture of SM12. The absorbers cause high-energy muons to multiple scatter and lose energy. Multiple scattering is mainly due to Coulomb scattering from the atomic nuclei, while energy loss is caused by several processes. The important mechanisms by which a muon (at our energies) loses energy in matter are ionization, bremsstrahlung, and pair production. We assumed that the muon track, upstream of the absorber, passed through the target center and the projected point in the absorber at an effective absorber scattering plane.[20] The track momentum was assumed to be that determined by SM3 plus an added correction for the average energy loss in the absorber.

Energy-loss distributions for muons in lead were calculated by integrating the mean energy-loss distributions in an infinitesimal piece of material. Figure 5 shows the energy-loss distributions for muons in 1.22 m of lead. The median values of these distributions were parametrized as a function of the incident muon energy E to obtain the energy-loss correction due to the lead wall. The fit gave

$$\Delta E_{\mathrm{Pb}} = 2.03 + 0.0105\,E\,, \tag{5}$$

where E and ΔE are in GeV. The Bethe-Bloch formula was used to correct for the mean ionization energy loss due to the polyethelene wall. It gave

$$\Delta E_{\mathrm{CH_2}} = 0.17 + 0.0002\,E\,. \tag{6}$$

The energy loss correction ΔE is just the sum $\Delta E_{\mathrm{CH_2}} + \Delta E_{\mathrm{Pb}}$. Once ΔE is known, the multiple-scattering angle can be obtained by iterating the traceback until the track converges to the target center while holding the effective scattering point at the absorber fixed. The starting point of the iteration assumes a multiple-scattering angle of zero. Two or three iterations were usually sufficient to achieve a traceback residual miss distance at the target center of less than 25 μm.

The above iteration procedure is only accurate for a statistical average of all tracks; individual muon trajectories upstream of the absorber wall might differ significantly from the trajectory iterated to the target center. In order to rid the data set of muons that had scattered off the beam dump and walls of the magnet, trajectories from the last iteration were required to be inside a nominal SM12 fiducial volume (smaller than the actual clear aperture). The dump cut was extended to $\pm$ 15.75 cm (5.4 mm outside the physical dump), and the angular aperture in the x-z plane was reduced from 2.7° to 2.5°, rejecting each track for which the x coordinate at the absorber effective scattering plane was larger than 35.6 cm in absolute value. It is possible that some muons might have suffered a much larger than average energy loss or multiple scattering in the absorbers, resulting in a very large miss distance at the target center when traced without the scattering angle correction. To eliminate large scatters, noniterated tracks were required to project within a target spot of $|x_t| \leq 12.7$ cm and $|y_t| \leq 12.7$ cm at $z_t = -3.30$ m.

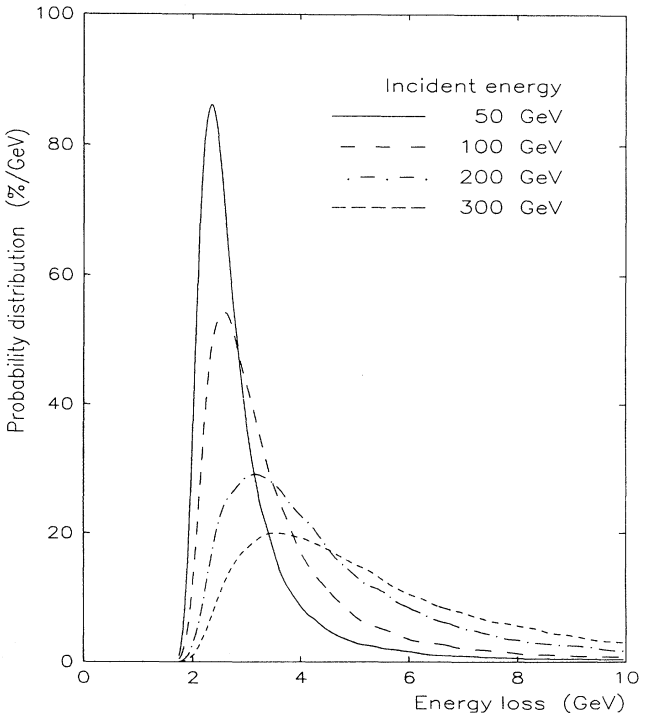

FIG. 5. Energy-loss distributions for muons traversing 122 cm of lead.

1. *Cut summary and efficiencies*

The complete set of cuts applied to the final sample of events can be summarized as follows.

a. Trigger selection. Only SINK triggers accepted by the trigger processor were considered for further analysis. Since the trigger efficiency depended strongly on the hodoscopes, care was taken to keep each hodoscope efficiency high (usually 99%) during the run. See Table IV for the average hodoscope efficiency and Table V for the efficiency of the SINK components. We assume[21] that

TABLE IV. Average hodoscope efficiencies.

Plane	4000 A	2750 A
X1	0.973 ± 0.001	0.982 ± 0.001
Y1	0.997 ± 0.000	0.999 ± 0.000
Y2	0.999 ± 0.000	0.999 ± 0.000
X3	0.991 ± 0.001	0.995 ± 0.001
Y3	0.993 ± 0.001	0.988 ± 0.001
X4	0.984 ± 0.001	0.996 ± 0.001
Y4	0.990 ± 0.000	0.958 ± 0.002

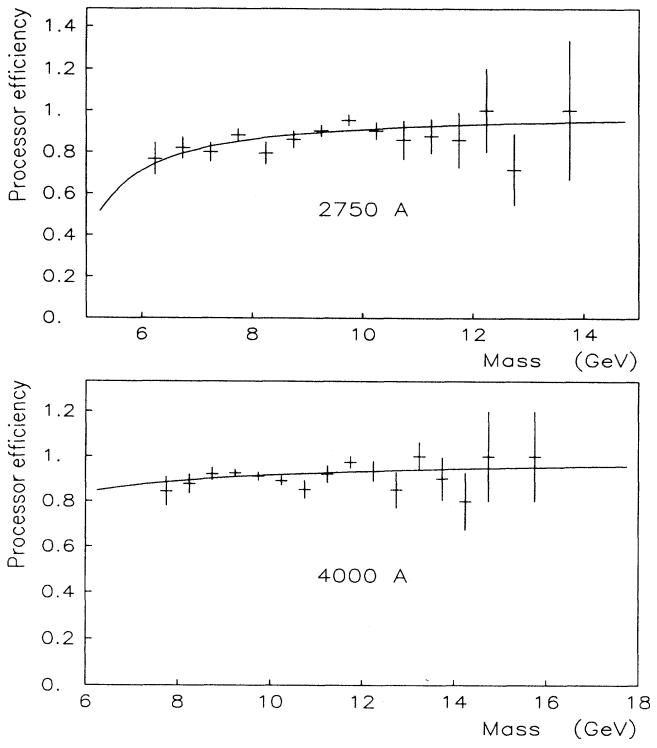

FIG. 6. Trigger processor efficiency vs mass.

the matrix and 2X4 efficiencies for the 2750-A data were the same as those of the 4000-A data. Thus, the overall SINK efficiency was $(95.3 \pm 0.7)\%$ for the 4000-A data and $(95.8 \pm 0.7)\%$ for the 2750-A data.

The trigger processor efficiency had a slight mass dependence at low mass due to the processor mass threshold, as shown in Fig. 6. This dependence was parametrized by fitting a polynomial to the data points. The data were then corrected as a function of mass using the fit function. Averaged over mass, the trigger processor efficiency was $(90.5 \pm 0.8)\%$ for the 4000-A data, and $(85.5 \pm 1.3)\%$ for the 2750-A data.

b. Multiplicity cuts. Events were rejected if they had more than 45 hodoscope hits, or more than 30 processor tracks, or more than 6 matrix roads. The combined efficiencies of these cuts was greater than 99.5% for the two data sets.

c. Tracking requirements. A minimum of 13 chamber hits out of 22 along each track were required. The tracking efficiency per track was calculated by folding the chamber efficiencies with the requirements of the track-finding algorithm yielding 94% for the 4000-A data and 95% for the 2750-A data.

TABLE V. Trigger efficiencies.

Element	4000 A	2750 A
Matrices	0.975 ± 0.005	
2X4	0.997 ± 0.002	
$\overline{\text{NX1}}$	0.981 ± 0.004	0.987 ± 0.004
$\overline{\text{NX3}}$	0.999 ± 0.001	0.999 ± 0.001
SINK	0.953 ± 0.007	

TABLE VI. Reconstruction efficiencies.

	4000 A	2750 A
Tracking	0.992 ± 0.001	0.991 ± 0.001
Station 0	0.949 ± 0.002	0.960 ± 0.003
Muon selection	1.000 ± 0.000	1.000 ± 0.000
Matrix roads	0.999 ± 0.001	0.999 ± 0.001
Processor tracks	0.999 ± 0.001	0.999 ± 0.001
Hodo multiplicity	0.997 ± 0.002	0.999 ± 0.001

d. Muon selection. A good muon track was required to have registered in at least three of the five detectors at station 4. The muon selection was essentially 100% efficient.

e. Muon pairs. The overall dimuon reconstruction efficiency included the efficiencies for track finding and muon selection. These efficiencies are listed in Table VI. The overall reconstruction efficiencies for two target muons were $(88.2 \pm 0.4)\%$ and $(90.5 \pm 0.5)\%$ for the 4000-A data and 2750-A data, respectively.

f. Geometrical cuts. To make sure that tracks went through regions of high detection efficiency, a cut (of 2.54 cm) was made on the projected track inside the edges of both the X4 and Y4 hodoscope planes. A second cut (of ± 2.54 cm) in the central region at X4 defined clearly the left and right sides of the apparatus. The SM12 fiducial volume was defined by the cuts outlined above in the iteration discussion.

g. Trigger requirements. Since our dimuon trigger required the matrix and 2X4 triggers to be set, only dimuon tracks that passed through trigger elements that satisfy these requirements were retained.

h. Spill quality selection. Only good accelerator spills, defined as those which had a targeting fraction greater than 70% and a live time greater than 50%, were included in the analysis.

B. Normalization

Figure 7 shows the raw mass spectra of our two data sets. The final 4000-A data sample contained 43 663 dimuon events, while the 2750-A data contained 19 470 dimuon events. To transform these samples into differential cross sections per nucleon we use the following definition. If Ω represents any kinematic variable, and $\langle\Omega\rangle$ its mean value in the interval $\Delta\Omega$, then

$$\left.\frac{d\sigma}{d\Omega}\right|_{\Omega=\langle\Omega\rangle} \equiv \frac{1}{\mathcal{L}} \frac{N_{\text{ev}}}{a\epsilon} \frac{1}{\Delta\Omega} \tag{7}$$

is the measured *average cross section*, where N_{ev} is the raw number of events in $\Delta\Omega$, a is the acceptance, ϵ is

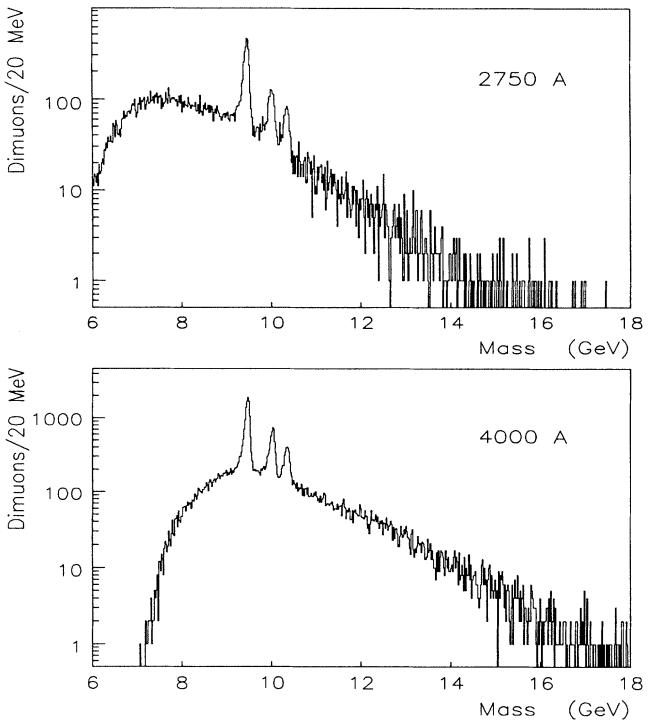

FIG. 7. Raw mass spectra of our two independent data sets.

the detection efficiency, and $\mathcal{L}$ is the integrated luminosity per nucleon. The following paragraphs describe the luminosity measurement and the acceptance calculation.

1. Integrated luminosity

The integrated luminosity per target nucleon, corrected for absorption of the incident beam and assuming an A^1 dependence of the cross section on the atomic weight A, is given by

$$\mathcal{L} = N_0 \rho \lambda (1 - e^{-L/\lambda}) N_{\rm inc} T_{\rm eff} , \tag{8}$$

where N_0 is Avogadro's number; ρ and L are the density and length of target, respectively; λ is the hadronic absorption length of the target material; $N_{\rm inc}$ is the number of incident protons; and $T_{\rm eff}$ is the fraction of the beam intercepted by the target. The average targeting fraction per spill was $(86 \pm 3)\%$ for the 10-mil target, and $(95 \pm 3)\%$ for the 17-mil target.

The integrated luminosity also had to be corrected for interactions that occurred during trigger or readout electronic dead time from a previous interaction. This live-time correction was $(89 \pm 3)\%$ for the 4000-A data and $(82 \pm 4)\%$ for the 2750-A data.

Taking into account the above factors, the integrated luminosities were $(1.14 \pm 0.08) \times 10^{42}$ nucleon/cm^2 and $(2.7 \pm 0.2) \times 10^{41}$ nucleon/cm^2 for the 4000-A and 2750-A data, respectively.

2. Acceptance

The acceptance is the fraction of the dimuons produced in the target which traverse the active area of the spectrometer and satisfy the trigger hodoscope requirements. It was evaluated by the Monte Carlo method using a form for the cross section indicated in Table VII and a software simulation of the apparatus. The simulation included all multiple-scattering and energy-loss effects, an accurate geometrical survey of the apparatus, and trigger hodoscope and matrix requirements. It did not include either the trigger processor simulation or efficiency corrections. We followed the radiative-correction calculation of Soni[22] to correct for higher-order QED radiative effects in dimuon production.

Muon pairs were generated over the phase space shown in Table VII. Those pairs that traced through the spectrometer successfully were recorded and an emulation of a raw data tape was produced. These Monte Carlo events were then analyzed as if they were real data, except for the cuts corresponding to the trigger processor.

Since the acceptance is the ratio of the Monte Carlo–accepted events to the generated events, it is important that the shape of the assumed cross section closely represents that of the real cross section. This was achieved by fitting distributions of reconstructed Monte Carlo events to those of real data events in an iterative procedure which converged once self-consistent results were obtained. In all cases, we integrated over the decay an-

TABLE VII. Distributions used for the simulation of dimuon events of mass m and momentum (p_t, ϕ, p_l) in the c.m. frame. The Collins-Soper [J. C. Collins and D. E. Soper, Phys. Rev. D 16, 2219 (1977)] convention is used to specify the μ^+ angles ($\theta_{\rm CS}$, $\phi_{\rm CS}$) in the dimuon c.m. frame, and $\tau = m^2/s$, $x_F = (1-\tau)x'_F = 2p_l/\sqrt{s}$, $p_t^{\rm max} = (\sqrt{s}/2)[(1-\tau)^2 - x_F^2]^{1/2}$, and $\epsilon = (4\tau + x_F^2)^{1/2}$.

Variable	Range	Continuum	Upsilons
m (GeV)	$(6, 18.5)$	$e^{-.77m}$	$\delta(m - m_\Upsilon)$
x'_F	$(-1, 1)$	$(1 - x'_F)^4 (1 + x'_F)^5$	$(1 + \tau - \epsilon)^2/\epsilon$
p_t (GeV)	$(0, p_t^{\rm max})$	$p_t/[1 + (p_t/3)^2]^6$	$p_t/[1 + (p_t/3.7)^2]^6$
ϕ	$(0, 2\pi)$	uniform	uniform
$\cos\theta_{\rm CS}$	$(-1, 1)$	$1 + \cos^2\theta_{\rm CS}$	uniform
$\phi_{\rm CS}$	$(0, \pi)$	uniform	uniform

gular distributions of the muon pair because the acceptance was restricted to a small range of the decay angle θ_{CS} near 90°. We used the Drell-Yan prediction of a $1+\cos^2\theta_{CS}$ decay angular distribution for the continuum and an isotropic decay distribution for Υ.

Figures 8 and 9 show the acceptance functions for the continuum and Υ, respectively, in selected ranges of the kinematical variables of interest. A simple exponential form was assumed for the continuum production cross section. The p_t distribution was determined from our measured invariant cross sections. These were fit with the form used by Kaplan *et al.*:[23]

$$E\frac{d^3\sigma}{d^3p} \propto \frac{1}{[1+(p_t/p_0)^2]^6} . \tag{9}$$

The values of p_0 were 3 and 3.7 GeV for the continuum and Υ, respectively. The x_F distribution for the continuum was calculated from a phenomenological fit to previous experiments,[24] and the x_F distribution for Υ came from the fusion of two gluons assuming a $x^{-1}(1-x)^2$ gluon distribution function in nucleons. Since we present cross sections differential in x_F (or rapidity in some cases), the assumed shape in this variable does not influence the measured cross section.

3. Backgrounds

The cuts used in the analysis enabled the majority of background events to be rejected. Most hadrons were absorbed in the lead wall before they could decay. Dimuons produced by independent interactions in the target were eliminated by the use of fast (single rf bucket resolution) trigger logic and the requirement in the analysis that the hodoscope latch pattern match the trigger requirements. The other possible source of background events was the vast number of muons produced in the beam dump. The trace-back cuts were accurate enough to distinguish dump muons from target muons. This was confirmed by analyzing runs taken with the target removed; no valid target dimuons were found. Furthermore, a search for same-sign muon pairs in data taken with a special trigger yielded no events. We therefore assume all sources of background events are negligible.

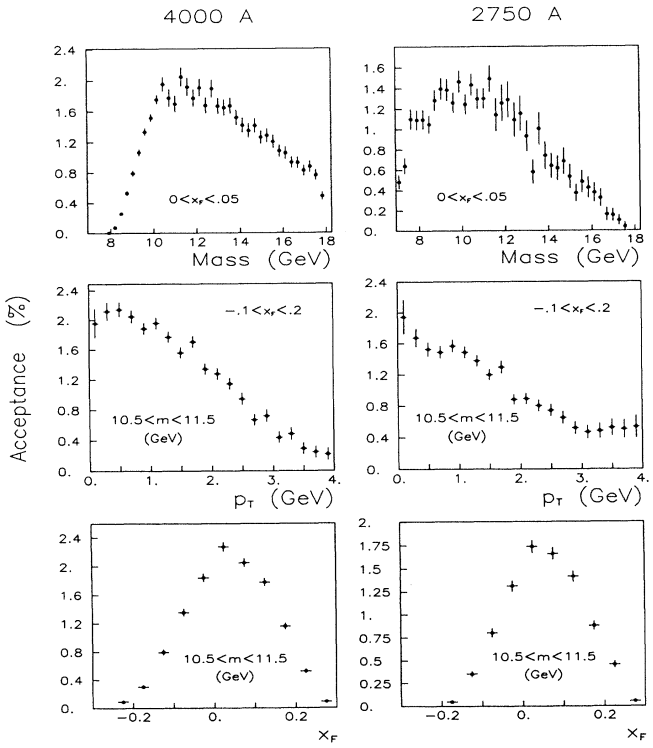

FIG. 8. Continuum acceptance functions in the intervals shown.

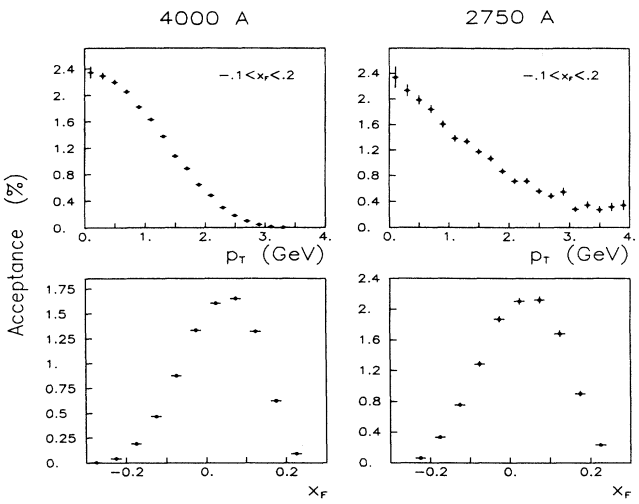

FIG. 9. Υ acceptance functions in the intervals shown.

IV. RESULTS

A. Introduction

The results are described in two sections, one for the continuum and the other for the Υ. To extract the Drell-Yan cross sections, the mass interval 9–10.5 GeV was omitted from the analysis to avoid Υ contamination. Drell-Yan fits were then used to subtract the dimuon continuum in the Υ region to obtain the corresponding resonance cross sections. We have assumed a linear dependence of the cross section on the atomic weight of our copper target, and we did not correct our data for nuclear Fermi motion in the target.[25]

Cross sections are presented as functions of one or two of the kinematical variables m, p_t, x_F, and y. An integration over the two production angular variables of the dimuon state and the two angular variables of the subsequent decay into two muons was performed. Because the range of angles accepted by the spectrometer is narrow, the analysis must assume a shape for the angular depen-

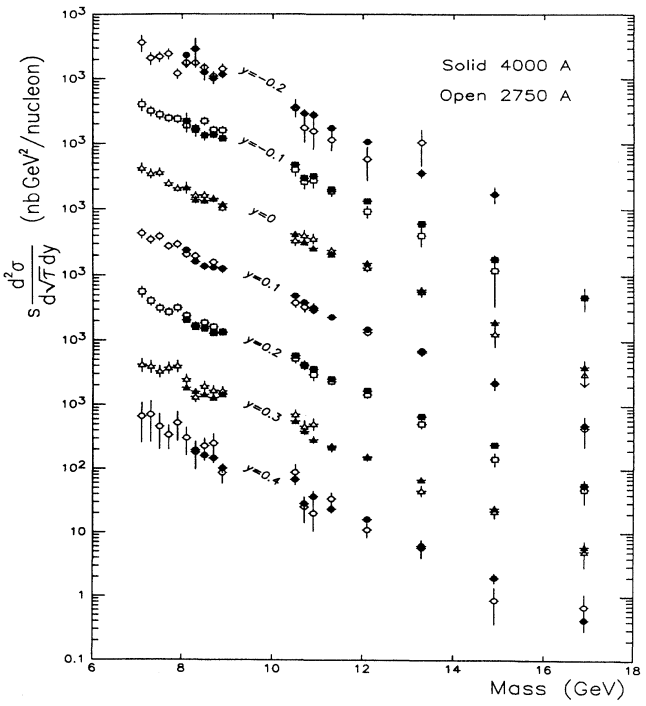

FIG. 10. Scaling form of the dimuon yield, excluding the Υ's, showing the agreement of the two sets in the region of overlap. The average of both sets is given in Table VIII.

dence of the process. The errors quoted throughout include only the statistical error of the data combined with the statistical error of the acceptance Monte Carlo calculation. There is an overall normalization error of about 15% and a point-to-point systematic error estimated to be about 10%.

The normalization error depends on the errors associated with luminosity and efficiency measurements. The point-to-point systematic error was estimated as follows. We have measured dimuon production at two different SM12 magnet currents with overlapping mass coverage. Each set was independently normalized. The ratio of the two measurements in the overlapping interval gives an estimate of the point-to-point errors. This comparison is shown in Fig. 10 as a scaling plot of the cross section versus mass for different rapidity bins. Figure 11 plots $d^2\sigma/dm\,dx_F$ and the ratio of the 2750-A to the 4000-A cross sections versus mass. Excluding the Υ region,[26] the overall ratio is 1.01 ± 0.05 but the ratio tends to vary systematically from 10% high at lower mass to 10% low at higher masses as shown in the inset of Fig. 11. One can also define a quantitative measure of the point-to-point systematic error. A 5% systematic point-to-point error, added in quadrature to the statistical error of each data point used in forming the ratio, yields a χ^2 per degree of freedom of unity for the ratio of the two data sets. Global comparisons of this data to other data sets may be less sensitive to any systematic variations in the data if such

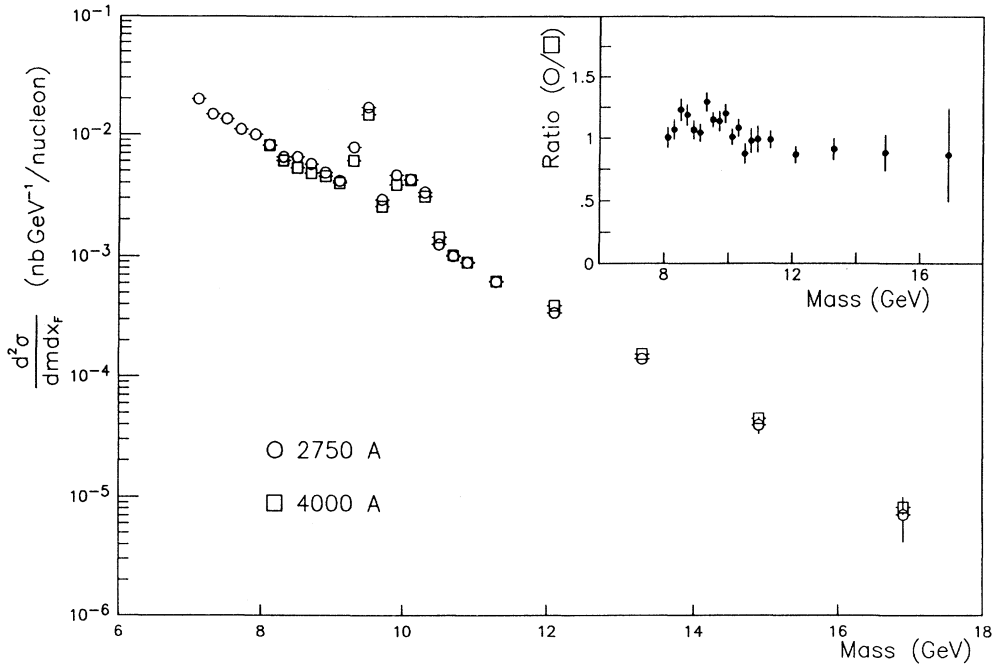

FIG. 11. Dimuon yield as a function of mass for the two data sets. The cross section is calculated using the dimuon continuum acceptance. The inset shows the ratio of both sets.

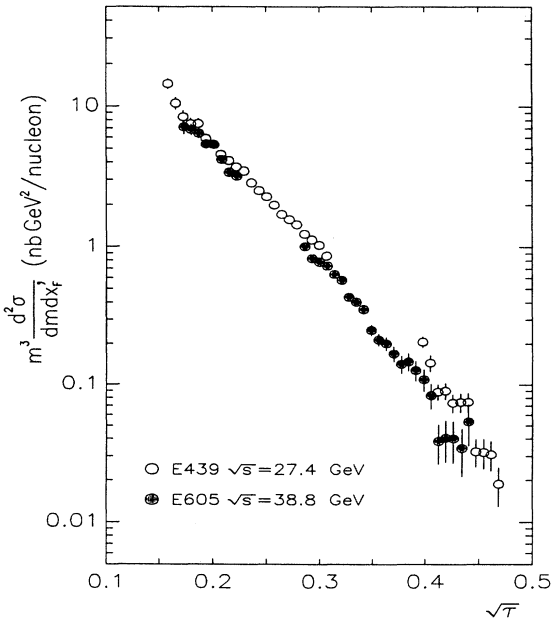

FIG. 12. Scaling form of the dimuon yield versus $\sqrt{\tau}$ comparing this experiment with experiment E439 (Smith *et al.*, Ref. 31, $\sqrt{s} = 27.4$ GeV) for the interval $0 < x_F' < .2$.

a 5% additional error is added quadratically to each data point.

The results presented in the following sections correspond to the weighted average of our two data sets. Data tables of the individual data sets can be found in Ref. 27.

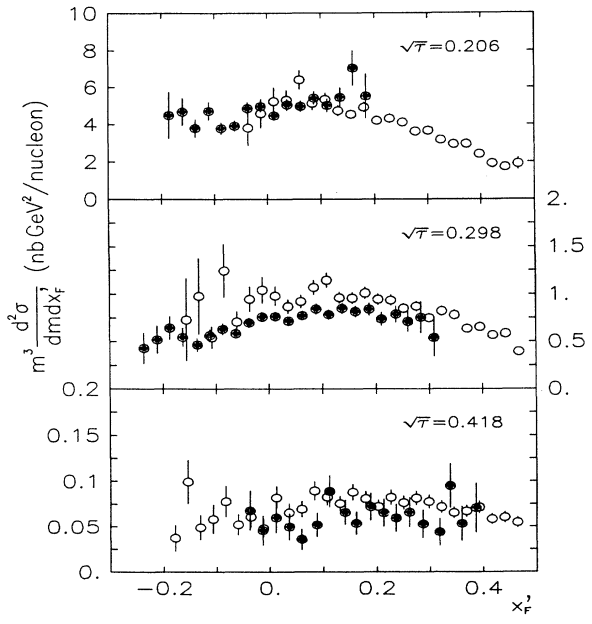

FIG. 13. Scaling form of the dimuon yield versus x_F' for different $\sqrt{\tau}$ bins, including a comparison of the data of Smith *et al.* (Ref. 31) taken at $\sqrt{s} = 27.4$ GeV. The symbols are the same as those of Fig. 12.

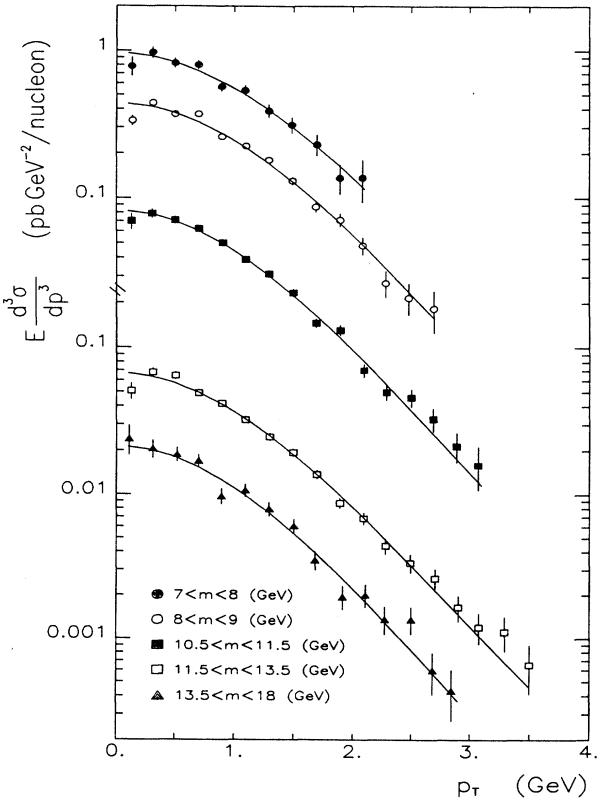

FIG. 14. Continuum dimuon p_t distributions for different mass bins. The lines correspond to the fit function described in the text.

B. Drell-Yan cross sections

1. Scaling comparisons

In addition to scaling comparisons with the data of Ito *et al.*[28] and Badier *et al.*[29] already presented in Ref. 30,

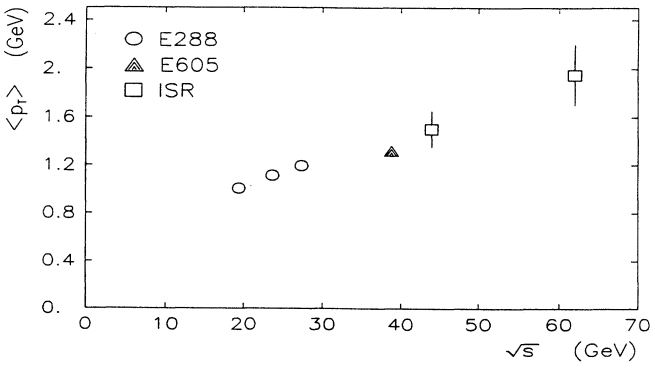

FIG. 15. Average transverse momentum of dimuons at $\sqrt{\tau} \simeq 0.3$ versus $\sqrt{s}$ for this experiment. Also shown are the data of Ref. 33 and Ref. 34.

TABLE VIII. Scaling form of the dimuon cross section $s\,d^2\sigma/d\sqrt{\tau}\,dy$ (σ) versus $\sqrt{\tau}$ for bins of rapidity (y), in units of nb GeV^2/nucleon. E+n denotes $\times 10^n$.

$\sqrt{\tau}$	$y = -0.2$	$y = -0.1$
0.1831	0.364E+03± 0.106E+03	0.399E+03± 0.851E+02
0.1883	0.209E+03± 0.459E+02	0.315E+03± 0.555E+02
0.1935	0.220E+03± 0.403E+02	0.277E+03± 0.454E+02
0.1986	0.243E+03± 0.455E+02	0.244E+03± 0.350E+02
0.2038	0.119E+03± 0.215E+02	0.237E+03± 0.354E+02
0.2089	0.176E+03± 0.312E+02	0.192E+03± 0.249E+02
0.2141	0.174E+03± 0.285E+02	0.166E+03± 0.192E+02
0.2192	0.140E+03± 0.198E+02	0.161E+03± 0.179E+02
0.2244	0.105E+03± 0.134E+02	0.145E+03± 0.129E+02
0.2296	0.123E+03± 0.139E+02	0.127E+03± 0.104E+02
0.2708	0.349E+02± 0.432E+01	0.456E+02± 0.395E+01
0.2760	0.289E+02± 0.431E+01	0.289E+02± 0.304E+01
0.2812	0.274E+02± 0.433E+01	0.309E+02± 0.320E+01
0.2915	0.162E+02± 0.162E+01	0.199E+02± 0.135E+01
0.3121	0.107E+02± 0.110E+01	0.125E+02± 0.828E+00
0.3431	0.357E+01± 0.566E+00	0.580E+01± 0.470E+00
0.3843	0.170E+01± 0.467E+00	0.179E+01± 0.272E+00
0.4359		0.474E+00± 0.180E+00

$\sqrt{\tau}$	$y = 0$	$y = 0.1$
0.1831	0.424E+03± 0.771E+02	0.431E+03± 0.753E+02
0.1883	0.350E+03± 0.577E+02	0.347E+03± 0.525E+02
0.1935	0.363E+03± 0.557E+02	0.386E+03± 0.585E+02
0.1986	0.248E+03± 0.340E+02	0.274E+03± 0.366E+02
0.2038	0.208E+03± 0.269E+02	0.294E+03± 0.394E+02
0.2089	0.212E+03± 0.234E+02	0.223E+03± 0.194E+02
0.2141	0.148E+03± 0.133E+02	0.169E+03± 0.127E+02
0.2192	0.144E+03± 0.119E+02	0.137E+03± 0.991E+01
0.2244	0.143E+03± 0.111E+02	0.137E+03± 0.928E+01
0.2296	0.114E+03± 0.769E+01	0.126E+03± 0.799E+01
0.2708	0.397E+02± 0.305E+01	0.460E+02± 0.325E+01
0.2760	0.331E+02± 0.280E+01	0.370E+02± 0.293E+01
0.2812	0.274E+02± 0.242E+01	0.302E+02± 0.258E+01
0.2915	0.216E+02± 0.130E+01	0.231E+02± 0.139E+01
0.3121	0.151E+02± 0.903E+00	0.147E+02± 0.884E+00
0.3431	0.605E+01± 0.372E+00	0.700E+01± 0.420E+00
0.3843	0.186E+01± 0.194E+00	0.224E+01± 0.176E+00
0.4359	0.404E+00± 0.101E+00	0.495E+00± 0.853E−01

$\sqrt{\tau}$	$y = 0.2$	$y = 0.3$
0.1831	0.560E+03± 0.110E+03	0.419E+03± 0.988E+02
0.1883	0.405E+03± 0.644E+02	0.396E+03± 0.897E+02
0.1935	0.315E+03± 0.498E+02	0.331E+03± 0.702E+02
0.1986	0.274E+03± 0.394E+02	0.377E+03± 0.793E+02
0.2038	0.318E+03± 0.477E+02	0.401E+03± 0.848E+02
0.2089	0.214E+03± 0.167E+02	0.193E+03± 0.171E+02
0.2141	0.162E+03± 0.110E+02	0.153E+03± 0.127E+02
0.2192	0.159E+03± 0.107E+02	0.151E+03± 0.126E+02
0.2244	0.135E+03± 0.914E+01	0.134E+03± 0.104E+02
0.2296	0.133E+03± 0.843E+01	0.149E+03± 0.116E+02
0.2708	0.571E+02± 0.399E+01	0.595E+02± 0.531E+01
0.2760	0.411E+02± 0.342E+01	0.403E+02± 0.435E+01
0.2812	0.345E+02± 0.296E+01	0.313E+02± 0.344E+01
0.2915	0.251E+02± 0.151E+01	0.232E+02± 0.160E+01
0.3121	0.164E+02± 0.981E+00	0.159E+02± 0.957E+00
0.3431	0.643E+01± 0.386E+00	0.630E+01± 0.449E+00
0.3843	0.220E+01± 0.178E+00	0.238E+01± 0.223E+00
0.4359	0.560E+00± 0.878E−01	0.607E+00± 0.110E+00

TABLE VIII. (*Continued.*)

$\sqrt{\tau}$	$y = 0.4$
0.2141	0.198E+03± 0.333E+02
0.2192	0.173E+03± 0.268E+02
0.2244	0.149E+03± 0.256E+02
0.2296	0.986E+02± 0.148E+02
0.2708	0.711E+02± 0.113E+02
0.2760	0.287E+02± 0.661E+01
0.2812	0.368E+02± 0.808E+01
0.2915	0.247E+02± 0.303E+01
0.3121	0.146E+02± 0.155E+01
0.3431	0.614E+01± 0.709E+00
0.3843	0.195E+01± 0.342E+00
0.4359	0.423E+00± 0.142E+00

we compare here the scaling form

$$m^3 \frac{d^2\sigma}{dm\, dx'_F}\ , \tag{10}$$

versus $\sqrt{\tau}$, with the results of Smith *et al.*[31] In Fig. 12, our data tends to be lower than those of Smith *et al.* as $\sqrt{\tau}$ increases. The same behavior was also noted in our previous publication[30] when comparing our data to those of Ito *et al.*[28] and Badier *et al.*[29] Figure 13 shows the x'_F distributions for various $\sqrt{\tau}$ bins, where the linear scale amplifies the effect. The full statistical power of the various data sets extends outside the overlap regions in any particular kinematical variable. Hence, a full global analysis using an order-α_s Drell-Yan formalism is needed to confirm that the trends seen exceed the normalization errors quoted by the various experiments.

Scaling forms of the cross section versus rapidity and x_F are presented in Tables VIII and IX, respectively. The ensemble of Drell-Yan data now available combined with the world data on deep-inelastic scattering should allow a more precise determination of the parton distributions in hadrons.[32]

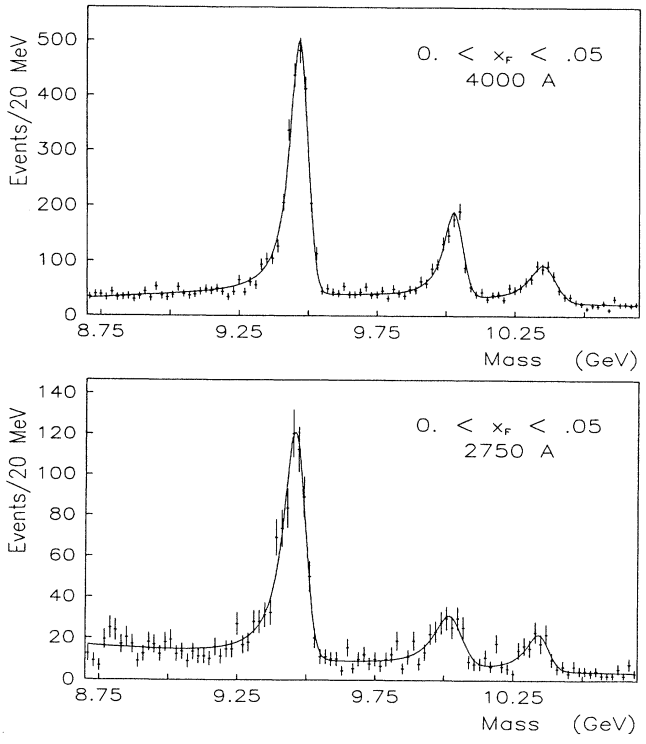

FIG. 16. The fit function used to extract Υ cross sections superimposed on the raw mass spectrum of the two data sets.

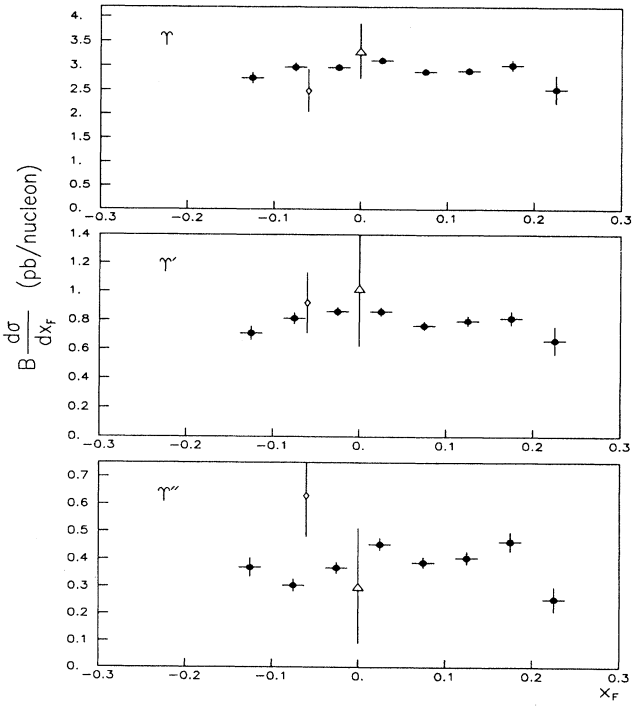

FIG. 17. Production cross section times branching fraction to lepton pairs for the three Υ S-states observed in this experiment. The triangles correspond to electron data[37] and the diamonds to muon data[38] measured previously with this spectrometer.

TABLE IX. Scaling form of the dimuon cross section $m^3 d^2\sigma/dm\,dx_F$ versus $\sqrt{\tau}$ for bins of x_F, in units of nb GeV^2/nucleon.

$\sqrt{\tau}$	$x_F = -0.125$	$x_F = -0.075$
0.1831	0.872E+01± 0.322E+01	0.565E+01± 0.119E+01
0.1897	0.499E+01± 0.121E+01	0.397E+01± 0.609E+00
0.1974	0.439E+01± 0.102E+01	0.483E+01± 0.657E+00
0.2038	0.399E+01± 0.839E+00	0.287E+01± 0.368E+00
0.2117	0.318E+01± 0.565E+00	0.377E+01± 0.460E+00
0.2188	0.417E+01± 0.784E+00	0.277E+01± 0.284E+00
0.2264	0.230E+01± 0.312E+00	0.323E+01± 0.275E+00
0.2338	0.283E+01± 0.312E+00	0.306E+01± 0.223E+00
0.2772	0.940E+00± 0.141E+00	0.105E+01± 0.112E+00
0.2847	0.106E+01± 0.163E+00	0.827E+00± 0.887E−01
0.2917	0.804E+00± 0.144E+00	0.866E+00± 0.980E−01
0.2994	0.392E+00± 0.827E−01	0.786E+00± 0.103E+00
0.3069	0.462E+00± 0.102E+00	0.640E+00± 0.102E+00
0.3201	0.411E+00± 0.587E−01	0.477E+00± 0.455E−01
0.3428	0.232E+00± 0.446E−01	0.337E+00± 0.396E−01
0.3741	0.188E+00± 0.485E−01	0.131E+00± 0.292E−01
0.3993		0.704E−01± 0.268E−01

$\sqrt{\tau}$	$x_F = -0.025$	$x_F = 0.025$
0.1825	0.660E+01± 0.995E+00	0.720E+01± 0.894E+00
0.1897	0.712E+01± 0.922E+00	0.722E+01± 0.861E+00
0.1969	0.413E+01± 0.439E+00	0.580E+01± 0.638E+00
0.2041	0.456E+01± 0.482E+00	0.439E+01± 0.360E+00
0.2116	0.444E+01± 0.391E+00	0.414E+01± 0.282E+00
0.2192	0.418E+01± 0.309E+00	0.319E+01± 0.192E+00
0.2264	0.322E+01± 0.208E+00	0.331E+01± 0.199E+00
0.2336	0.328E+01± 0.197E+00	0.297E+01± 0.178E+00
0.2773	0.127E+01± 0.103E+00	0.120E+01± 0.856E−01
0.2844	0.118E+01± 0.101E+00	0.987E+00± 0.781E−01
0.2917	0.786E+00± 0.727E−01	0.784E+00± 0.683E−01
0.2987	0.810E+00± 0.809E−01	0.833E+00± 0.735E−01
0.3064	0.689E+00± 0.772E−01	0.761E+00± 0.702E−01
0.3199	0.594E+00± 0.422E−01	0.624E+00± 0.387E−01
0.3430	0.351E+00± 0.316E−01	0.294E+00± 0.239E−01
0.3760	0.141E+00± 0.255E−01	0.184E+00± 0.240E−01
0.4044	0.764E−01± 0.222E−01	0.830E−01± 0.192E−01

$\sqrt{\tau}$	$x_F = 0.075$	$x_F = 0.125$
0.1824	0.853E+01± 0.124E+01	0.505E+01± 0.102E+01
0.1896	0.726E+01± 0.891E+00	0.807E+01± 0.161E+01
0.1970	0.470E+01± 0.492E+00	0.608E+01± 0.100E+01
0.2045	0.575E+01± 0.419E+00	0.490E+01± 0.383E+00
0.2116	0.414E+01± 0.249E+00	0.366E+01± 0.237E+00
0.2188	0.376E+01± 0.226E+00	0.346E+01± 0.216E+00
0.2262	0.335E+01± 0.201E+00	0.341E+01± 0.205E+00
0.2333	0.324E+01± 0.195E+00	0.323E+01± 0.194E+00
0.2770	0.138E+01± 0.100E+00	0.139E+01± 0.107E+00
0.2845	0.118E+01± 0.917E−01	0.120E+01± 0.986E−01
0.2915	0.107E+01± 0.844E−01	0.114E+01± 0.998E−01
0.2992	0.884E+00± 0.777E−01	0.806E+00± 0.779E−01
0.3064	0.779E+00± 0.750E−01	0.799E+00± 0.801E−01
0.3199	0.600E+00± 0.372E−01	0.639E+00± 0.413E−01
0.3433	0.388E+00± 0.267E−01	0.338E+00± 0.260E−01
0.3729	0.190E+00± 0.207E−01	0.191E+00± 0.209E−01
0.4010	0.925E−01± 0.180E−01	0.108E+00± 0.169E−01
0.4367	0.519E−01± 0.144E−01	0.333E−01± 0.106E−01

TABLE IX. (*Continued.*)

$\sqrt{\tau}$	$x_F = 0.175$	$x_F = 0.225$
0.2045	0.393E+01± 0.873E+00	
0.2120	0.339E+01± 0.465E+00	
0.2189	0.374E+01± 0.419E+00	
0.2260	0.269E+01± 0.271E+00	
0.2334	0.281E+01± 0.261E+00	0.310E+01± 0.112E+01
0.2771	0.137E+01± 0.142E+00	0.103E+01± 0.203E+00
0.2843	0.114E+01± 0.120E+00	0.104E+01± 0.167E+00
0.2915	0.876E+00± 0.958E−01	0.886E+00± 0.147E+00
0.2988	0.980E+00± 0.110E+00	0.848E+00± 0.139E+00
0.3064	0.752E+00± 0.885E−01	0.783E+00± 0.124E+00
0.3198	0.642E+00± 0.469E−01	0.569E+00± 0.583E−01
0.3450	0.295E+00± 0.266E−01	0.356E+00± 0.355E−01
0.3737	0.205E+00± 0.255E−01	0.225E+00± 0.279E−01
0.4054	0.114E+00± 0.207E−01	0.909E−01± 0.196E−01
0.4347	0.486E−01± 0.131E−01	0.425E−01± 0.128E−01
	$x_F = 0.275$	
0.2998	0.946E+00± 0.371E+00	
0.3062	0.532E+00± 0.175E+00	
0.3205	0.370E+00± 0.742E−01	
0.3461	0.258E+00± 0.413E−01	
0.3731	0.144E+00± 0.307E−01	
0.4027	0.122E+00± 0.276E−01	
0.4318	0.364E−01± 0.138E−01	

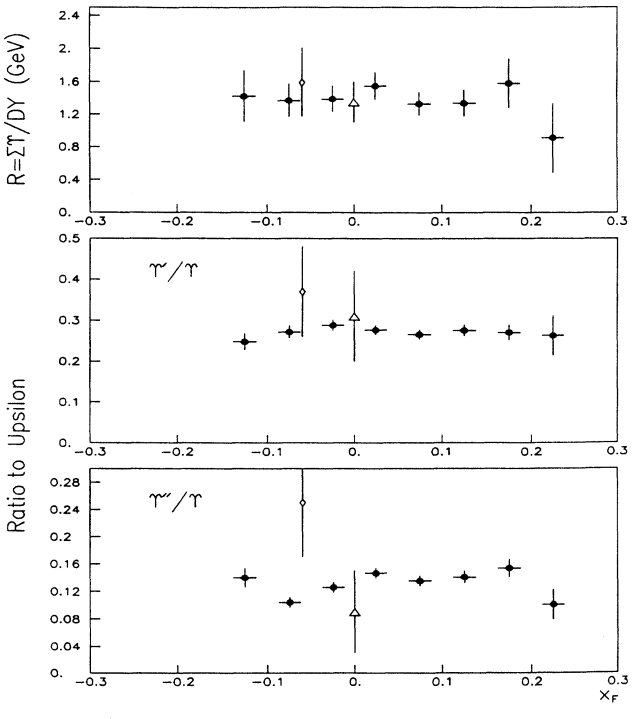

FIG. 18. The Υ to continuum ratio R defined by Eq. (12), and the relative yield of Υ′ to Υ and Υ″ to Υ. The triangles correspond to electron data (Ref. 37) and the diamonds to muon data (Ref. 38) measured previously with this spectrometer.

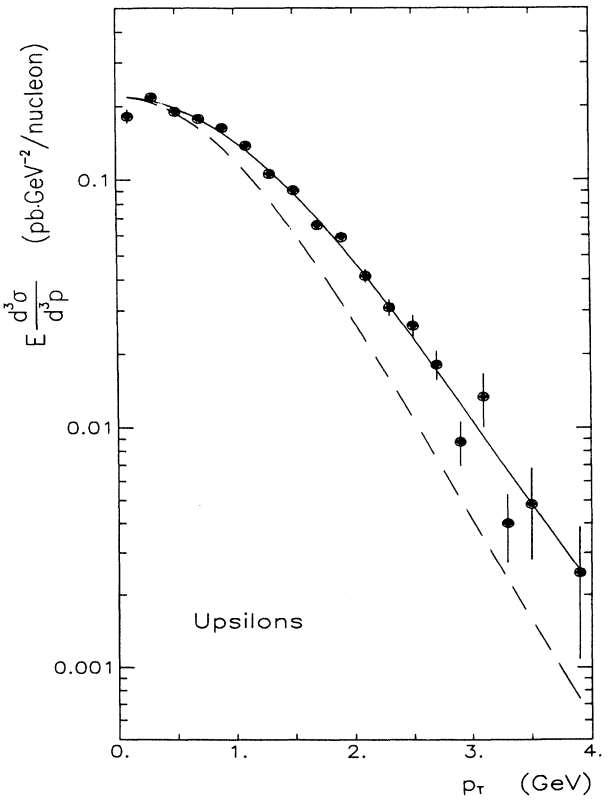

FIG. 19. p_t distribution for the sum of the three Υ's. The solid curve is a fit to the data, the dashed curve gives the shape of the continuum dimuons under the resonances (see text).

TABLE X. Invariant dimuon cross section ($E\,d^3\sigma/d^3p$) evaluated at x_F=0.1 as described in the text, in units of pb/GeV^2 nucleon. The Υ continuum subtraction is described in Sec. IV C 2.

p_t (GeV) \ Mass (GeV)	7–8	8–9
0.10	0.785E+00± 0.115E+00	0.333E+00± 0.333E+00
0.30	0.973E+00± 0.861E-01	0.439E+00± 0.439E+00
0.50	0.825E+00± 0.616E-01	0.368E+00± 0.368E+00
0.70	0.805E+00± 0.570E-01	0.370E+00± 0.370E+00
0.90	0.569E+00± 0.422E-01	0.259E+00± 0.259E+00
1.10	0.537E+00± 0.447E-01	0.224E+00± 0.224E+00
1.30	0.388E+00± 0.390E-01	0.180E+00± 0.180E+00
1.50	0.312E+00± 0.380E-01	0.131E+00± 0.131E+00
1.70	0.229E+00± 0.373E-01	0.875E-01± 0.875E-01
1.90	0.136E+00± 0.307E-01	0.713E-01± 0.713E-01
2.10	0.137E+00± 0.433E-01	0.482E-01± 0.482E-01
2.30		0.272E-01± 0.272E-01
2.50		0.217E-01± 0.217E-01
2.70		0.184E-01± 0.184E-01

p_t(GeV) \ Mass (GeV)	Υ (continuum subtracted)	10.5–11.5
0.10	0.182E+00± 0.114E-01	0.701E-01± 0.701E-01
0.30	0.217E+00± 0.846E-02	0.784E-01± 0.784E-01
0.50	0.190E+00± 0.637E-02	0.712E-01± 0.712E-01
0.70	0.178E+00± 0.528E-02	0.624E-01± 0.624E-01
0.90	0.164E+00± 0.463E-02	0.503E-01± 0.503E-01
1.10	0.138E+00± 0.403E-02	0.390E-01± 0.390E-01
1.30	0.106E+00± 0.340E-02	0.312E-01± 0.312E-01
1.50	0.909E-01± 0.325E-02	0.234E-01± 0.234E-01
1.70	0.661E-01± 0.280E-02	0.147E-01± 0.147E-01
1.90	0.591E-01± 0.284E-02	0.131E-01± 0.131E-01
2.10	0.414E-01± 0.249E-02	0.705E-02± 0.705E-02
2.30	0.309E-01± 0.238E-02	0.500E-02± 0.500E-02
2.50	0.262E-01± 0.254E-02	0.459E-02± 0.459E-02
2.70	0.182E-01± 0.245E-02	0.330E-02± 0.330E-02
2.90	0.876E-02± 0.180E-02	0.215E-02± 0.215E-02
3.10	0.134E-01± 0.330E-02	0.159E-02± 0.159E-02
3.30	0.400E-02± 0.127E-02	
3.50	0.482E-02± 0.201E-02	
3.90	0.247E-02± 0.139E-02	

2. p_t distributions

Invariant cross sections versus p_t are presented in Fig. 14 and Table X for several mass intervals and for the x_F interval (−0.1, 0.2). These were obtained by integrating the cross section over the indicated mass interval using the formula

$$\left\langle E\frac{d^3\sigma}{d^3p}\right\rangle = \frac{2E}{\pi\sqrt{s}}\,\frac{d^2\sigma}{dp_t^2\,dx_F}\,. \tag{11}$$

The curve superimposed on each distribution of Fig. 14 is a fit to the data points using the function given in Eq. (9). The fit parameters and average transverse momentum $\langle p_t\rangle$ are given in Table XI. Figure 15 shows $\langle p_t\rangle$ together with results from other experiments[33,34] as a function of $\sqrt{s}$. The observed increase of $\langle p_t\rangle$ with $\sqrt{s}$ is consistent with perturbative QCD calculations.[35] In the perturbative calculation, the increased transverse momentum occurs through higher-order gluon Compton scattering and gluon bremsstrahlung diagrams.

C. Υ cross sections

1. x_F dependence

To study the x_F dependence of the Υ cross section, the raw data were divided into several x_F bins and the

TABLE X. (*Continued.*)

p_t (GeV) \ Mass (GeV)	11.5–13.5	13.5–18.0
0.10	0.508E-01± 0.642E-02	0.240E-01± 0.240E-01
0.30	0.679E-01± 0.479E-02	0.206E-01± 0.206E-01
0.50	0.646E-01± 0.387E-02	0.188E-01± 0.188E-01
0.70	0.492E-01± 0.263E-02	0.171E-01± 0.171E-01
0.90	0.417E-01± 0.219E-02	0.973E-02± 0.973E-02
1.10	0.323E-01± 0.176E-02	0.107E-01± 0.107E-01
1.30	0.247E-01± 0.146E-02	0.791E-02± 0.791E-02
1.50	0.194E-01± 0.119E-02	0.605E-02± 0.605E-02
1.70	0.137E-01± 0.976E-03	0.350E-02± 0.350E-02
1.90	0.866E-02± 0.731E-03	0.194E-02± 0.194E-02
2.10	0.679E-02± 0.636E-03	0.200E-02± 0.200E-02
2.30	0.440E-02± 0.550E-03	0.136E-02± 0.136E-02
2.50	0.334E-02± 0.483E-03	0.136E-02± 0.136E-02
2.70	0.262E-02± 0.420E-03	0.600E-03± 0.600E-03
2.90	0.165E-02± 0.330E-03	0.435E-03± 0.435E-03
3.10	0.120E-02± 0.284E-03	
3.30	0.111E-02± 0.298E-03	
3.50	0.654E-03± 0.243E-03	

resulting mass spectrum was then fit with the sum of four functions representing the Drell-Yan yield and the three Υ yields. Figure 16 presents the overall fit superimposed on the raw mass spectra of our two data sets.

Figure 17 and Table XII show the production cross section times branching ratio to muon pairs, $B\,d\sigma/dx_F$, for each of the Υ near $x_F=0$. The ratios of the corresponding cross sections, Υ'/Υ and Υ''/Υ, are shown in Fig. 18 and Table XIII together with the Υ to continuum ratio defined[36] as

$$R=\sum_{V=\Upsilon,\Upsilon',\Upsilon''}\frac{B(V\rightarrow l^+l^-)\,(d\sigma/dx_F)(pN\rightarrow VX)}{(d^2\sigma/dm\,dx_F)(pN\rightarrow l^+l^-X)|_{m=m_\Upsilon}}\,. \tag{12}$$

These same quantities have previously been measured with the E605 spectrometer for both dielectron[37] and dimuon[38] events and are shown in the corresponding plots. In general, there is agreement among the three measurements with this spectrometer. The second error shown in Tables XII and XIII is an estimate of the systematic error introduced by the subtraction of the continuum fit from the resonance data.

It is interesting to observe that $B\,d\sigma/dx_F$ in Fig. 17 seems to be independent of x_F in the range shown, in contrast with the continuum cross section that has a positive slope near $x_F=0$, as shown in Fig. 13. If Υ production is realized through the strong interaction of quarks and gluons, isospin symmetry of the color force would imply that the Υ production cross section should be symmetric about $x_F=0$ in p-N collisions whereas the electromagnetic nature of the fundamental interaction in the Drell-Yan process leads to a forward asymmetry in p-N reactions.

TABLE XI. Parameters of the dimuon p_t distribution fit for the functional form $A/[1+(p_t/p_0)^2]^6$. Note that the mean transverse momentum $\langle p_t\rangle$ is almost mass independent (excluding the Υ's). A continuum subtraction was made in the Υ region as explained in the text.

Mass range (GeV)	A (pb/GeV^2)	p_0 (GeV)	$\langle p_t\rangle$ (GeV)
7–8	0.964±0.045	3.221±0.124	1.385±0.053
8–9	0.436±0.010	3.141±0.050	1.351±0.021
Υ	0.219±0.004	3.715±0.041	1.598±0.017
10.5–11.5	0.082±0.003	3.048±0.044	1.311±0.019
11.5–13.5	0.067±0.002	3.074±0.043	1.322±0.018
13.5–18.0	0.021±0.001	2.951±0.081	1.269±0.035

TABLE XII. Upsilon production cross section times dimuon branching ratio ($B\,d\sigma/dx_F$) versus x_F, in pb/nucleon. The first error is statistical and the second error is an estimate of the systematic error due to the fitting procedure.

Resonance	x_F	$Bd\sigma/dx_F$
Υ	−0.125	$2.745 \pm 0.115 \pm 0.482$
	−0.075	$2.966 \pm 0.085 \pm 0.325$
	−0.025	$2.959 \pm 0.067 \pm 0.242$
	0.025	$3.105 \pm 0.064 \pm 0.239$
	0.075	$2.879 \pm 0.061 \pm 0.243$
	0.125	$2.892 \pm 0.070 \pm 0.287$
	0.175	$3.011 \pm 0.108 \pm 0.390$
	0.225	$2.514 \pm 0.292 \pm 1.242$
Υ'	−0.125	$0.708 \pm 0.047 \pm 0.218$
	−0.075	$0.811 \pm 0.038 \pm 0.138$
	−0.025	$0.859 \pm 0.032 \pm 0.140$
	0.025	$0.859 \pm 0.030 \pm 0.144$
	0.075	$0.761 \pm 0.028 \pm 0.132$
	0.125	$0.795 \pm 0.033 \pm 0.157$
	0.175	$0.814 \pm 0.047 \pm 0.197$
	0.225	$0.660 \pm 0.094 \pm 0.433$
Υ''	−0.125	$0.369 \pm 0.034 \pm 0.115$
	−0.075	$0.304 \pm 0.022 \pm 0.111$
	−0.025	$0.368 \pm 0.020 \pm 0.072$
	0.025	$0.454 \pm 0.021 \pm 0.096$
	0.075	$0.388 \pm 0.019 \pm 0.095$
	0.125	$0.405 \pm 0.023 \pm 0.123$
	0.175	$0.463 \pm 0.035 \pm 0.146$
	0.225	$0.253 \pm 0.045 \pm 0.225$

TABLE XIII. Relative production ratios of Υ' to Υ and Υ'' to Υ, versus x_F. R is the Υ to dimuon continuum ratio defined in the text (R has the units GeV). The first error is statistical and the second error is an estimate of the systematic error due to the fitting procedure.

	x_F	Ratio
Υ'/Υ	−0.125	$0.248 \pm 0.020 \pm 0.027$
	−0.075	$0.271 \pm 0.015 \pm 0.012$
	−0.025	$0.288 \pm 0.013 \pm 0.020$
	0.025	$0.277 \pm 0.011 \pm 0.023$
	0.075	$0.265 \pm 0.011 \pm 0.021$
	0.125	$0.275 \pm 0.013 \pm 0.024$
	0.175	$0.270 \pm 0.018 \pm 0.026$
	0.225	$0.263 \pm 0.048 \pm 0.029$
Υ''/Υ	−0.125	$0.140 \pm 0.014 \pm 0.011$
	−0.075	$0.104 \pm 0.008 \pm 0.023$
	−0.025	$0.126 \pm 0.007 \pm 0.012$
	0.025	$0.146 \pm 0.007 \pm 0.018$
	0.075	$0.135 \pm 0.007 \pm 0.019$
	0.125	$0.140 \pm 0.009 \pm 0.026$
	0.175	$0.153 \pm 0.013 \pm 0.024$
	0.225	$0.101 \pm 0.022 \pm 0.027$
R	−0.125	$1.422 \pm 0.316 \pm 0.510$
	−0.075	$1.370 \pm 0.202 \pm 0.278$
	−0.025	$1.389 \pm 0.161 \pm 0.211$
	0.025	$1.550 \pm 0.168 \pm 0.227$
	0.075	$1.331 \pm 0.142 \pm 0.210$
	0.125	$1.338 \pm 0.163 \pm 0.249$
	0.175	$1.582 \pm 0.298 \pm 0.401$
	0.225	$0.909 \pm 0.424 \pm 0.753$

2. p_t distribution

The p_t distribution for Υ's was extracted from data in the mass ranges $9.36 < m < 9.54$ GeV (Υ), $9.92 < m < 10.12$ GeV (Υ'), and $10.26 < m < 10.48$ GeV (Υ''). The x_F range considered was $(-0.1, 0.2)$, and appropriate continuum subtraction and acceptance corrections were carried out at each Υ resonance. The results summed over the three resonances are shown in Fig. 19 as an invariant cross section versus p_t, along with a fit (solid curve) of the same form as used for the continuum data. The dashed curve shows the shape (p_0=3.1 GeV) of the continuum p_t distribution in the region of the Υ resonances. The cross section and fit parameters are tabulated together with the continuum results in Tables X and XI. An increased yield of Υ states at large values of p_t, compared with continuum Drell-Yan dimuons, is clear.

V. CONCLUSIONS

In summary, we have presented a high-statistics measurement of dimuon production in proton-copper collisions at $\sqrt{s} = 38.8$ GeV. A scaling form of the continuum cross section was compared with an experiment at $\sqrt{s} = 27.4$ GeV. This comparison and others[30] are consistent with predicted perturbative QCD scale violation effects. The three lowest-lying Υ states were clearly resolved and the corresponding cross sections times branching ratios to muon pairs were measured. The p_t and x_F distributions of Υ's are different from those of the continuum, indicating different production mechanisms.

ACKNOWLEDGMENTS

We would like to acknowledge the efforts of the Fermilab Research and Accelerator Divisions and funding from the U.S. Dept. of Energy, the National Science Foundation, and the Japanese Ministry of Education.

[a]Present address: Instituto de Fisica, Leon, Mexico.
[b]Present address: Northern Illinois University, DeKalb, IL 60115.
[c]Present address: University of Chicago, Chicago, IL 60637.
[d]Present address: Miyazaki University, Miyazaki, Japan.
[e]Present address: Okayama University, Okayama, Japan.
[f]Present address: Osaka City University, Osaka, Japan.
[g]Present address: University of Sydney, Sydney, Australia.
[h]Present address: University of California, Berkeley, CA 94720.
[i]Present address: University of Arizona, Tucson, AZ 85721.
[j]Present address: University of Illinois at Chicago, Chicago, IL 60680.
[k]Present address: Fermilab, Batavia, IL 60510.
[l]Present address: University of Bonn, Bonn, Federal Republic of Germany.
[m]Present address: Stanford Linear Accelerator Center, Stanford, CA 94309.

[1]J. H. Christenson *et al.*, Phys. Rev. Lett. **25**, 1523 (1970).
[2]S. D. Drell and T-M. Yan, Phys. Rev. Lett. **25**, 316 (1970).
[3]J. Aubert *et al.*, Phys. Rev. Lett. **33**, 1404 (1974).
[4]S. W. Herb *et al.*, Phys. Rev. Lett. **39**, 252 (1977); W. R. Innes *et al.*, *ibid.* **39**, 1240 (1977); K. Ueno *et al.*, *ibid.* **42**, 486 (1979).
[5]I. R. Kenyon, Rep. Prog. Phys. **45**, 1261 (1982); C. Grosso-Pilcher and M. J. Shochet, Annu. Rev. Nucl. Part. Sci. **36**, 1 (1986); J. P. Rutherfoord, in *Proceedings of the 1985 International Symposium on Lepton and Photon Interactions at High Energies*, Kyoto, Japan, 1985, edited by M. Konuma and K. Takahashi (RIFP, Kyoto, 1986).
[6]G. E. Hogan *et al.*, Phys. Rev. Lett. **42**, 948 (1979); K. J. Anderson *et al.*, *ibid.* **43**, 1219 (1979); R. Barate *et al.*, *ibid.* **43**, 1541 (1979); C. Kourkoumelis *et al.*, Phys. Lett. **91B**, 475 (1980); J. Badier *et al.*, Z. Phys. C **11**, 195 (1981).
[7]J. C. Peng *et al.*, in *Nuclear and Particle Physics on the Light Cone*, proceedings of the LAMPF Workshop, Los Alamos, 1988, edited by M. B. Johnson and L. S. Kisslinger (World Scientific, Singapore, 1989); D. M. Kaplan *et al.*, in *Proceedings of the Storrs Meeting*, Annual Meeting of the Division of Particles and Fields of the APS, Storrs, Connecticut, 1988, edited by K. Haller *et al.* (World Scientific, Singapore, 1989).
[8]J. Kubar *et al.*, Nucl. Phys. **B175**, 251 (1980); G. Altarelli, Phys. Rep. **81C**, 1 (1982).
[9]W. Buchmüller and S. Cooper, MIT Report MIT-LNS-159, 1987 (unpublished).
[10]R. Baier and R. Rückl, Z. Phys. C **19**, 251 (1983).
[11]J. A. Crittenden *et al.*, Phys. Rev. D **34**, 2584 (1986); also, see description of FNAL-E605 in *Major Detectors in Elementary Particle Physics* (Report No. LBL-91 Supplement).
[12]S. I. Baker *et al.*, Nucl. Instrum. Methods **222**, 467 (1984).
[13]R. W. Fast *et al.*, IEEE Trans. Magn. **17**, 1903 (1981).
[14]J. A. Crittenden *et al.*, IEEE Trans. Nucl. Sci. **NS-31**, 1028 (1984).
[15]R. Gray and J. P. Rutherfoord, Nucl. Instrum. Methods **A244**, 440 (1986).
[16]Logical operations AND and OR are denoted by $\odot$ and $\oplus$, respectively.
[17]Y. B. Hsiung, Ph.D. thesis, Columbia University, 1986.
[18]Y. B. Hsiung *et al.*, Nucl. Instrum. Methods **A245**, 338 (1986).
[19]R. E. Plaag and J. P. Rutherfoord, Nucl. Instrum. Methods **A273**, 177 (1986).
[20]It can be shown that, neglecting energy loss, the effective scattering plane is located on average $\frac{1}{3}$ of the distance through the absorber. See, for example, B. Rossi, *High Energy Particles* (Prentice-Hall, Englewood Cliffs, NJ, 1952).
[21]Because the prescaled trigger used to monitor the matrix and 2X4 elements was removed during the 2750-A running period, we were not able to measure either of those efficiencies for that data set. We measured constant hodoscope efficiencies during both runs and hence have assumed a constant efficiency for these requirements.
[22]A. Soni, Phys. Rev. D **8**, 2264 (1973).
[23]D. M. Kaplan *et al.*, Phys. Rev. Lett. **40**, 435 (1978).
[24]J. P. Rutherfoord, E605 Internal report, 1985 (unpublished).
[25]Since A-dependence measurements include Fermi motion in the target nucleus, we do not make a partial correction for this effect in our analysis.
[26]The data points in the Υ region of Fig. 11 are not corrected for the different acceptance for vector-meson decay or for the different resolutions at the two magnet currents.
[27]G. Moreno, Ph.D. thesis, CINVESTAV, Mexico, 1989.
[28]A. S. Ito *et al.*, Phys. Rev. D **23**, 604 (1981).
[29]J. Badier *et al.*, Z. Phys. C **26**, 489 (1985).
[30]C. N. Brown *et al.*, Phys. Rev. Lett. **63**, 2637 (1989).
[31]S. R. Smith *et al.*, Phys. Rev. Lett. **46**, 1607 (1981). The data points shown in this comparison were obtained from J. P. Rutherfoord.
[32]J. Morfin and W. Tung (private communication).
[33]J. K. Yoh *et al.*, Phys. Rev. Lett. **41**, 684 (1978).
[34]D. Antreasyan *et al.*, Phys. Rev. Lett. **47**, 12 (1981).
[35]H. Fritzsch and P. Minkowski, Phys. Lett. **73B**, 80 (1978); G. Altarelli, G. Parisi, and R. Petronzio, *ibid.* **76B**, 351 (1978); **76B**, 356 (1978).
[36]S. Childress *et al.*, Phys. Rev. Lett. **55**, 1962 (1985).
[37]T. Yoshida *et al.*, Phys. Rev. D **39**, 3516 (1989).
[38]R. Gray, Ph.D. thesis, University of Washington, 1988.